Enhanced Transient Performance of Wind-Driven PMSG: A Revised Control Structure of Wind-Power Converters

Muhammad Arif Sharafat ALI
Department of Electrical and Computer Engineering,
Sungkyunkwan University, Natural Sciences Campus, Suwon 440-746, Republic of Korea
sharafat@skku.edu

***Abstract*—To deal with low-voltage ride-through (LVRT) and to enhance the transient performance of a grid-connected wind-driven permanent-magnet synchronous generator during voltage dips on the grid side, this study presents a revised control structure for wind-power converters, comprising a machine-side converter (MSC) and grid-side converter (GSC). In the proposed approach, the control variables' references are modified with grid voltage, and the revised control designs for the MSC and GSC are established. During voltage dips, the captured wind power is stored as the kinetic energy of the turbine rotor. The active component of the stator current is curtailed according to the dip level by terminating the maximum power tracking operation. The modified GSC current references assist the grid in providing the required reactive current and attempt to minimize the power loss by utilizing the maximum GSC current-carrying capacity. The revised controls are responsible not only for maintaining the DC-link voltage and GSC current within safe limits, but also support the grid in providing reactive power during voltage recovery. Simulations verify the suitability and effectiveness of the proposed design in handling LVRT operations and providing additional flexibility by incorporating stability and security constraints.**

***Index Terms*—generators, power converters, power system faults, power system security, wind energy integration.**

I. Introduction

A. Background

The increased complexity of existing power systems owing to the massive penetration of wind-power plants (WPPs), which are intermittent and have a low inertial response, have significant impacts on the dynamic behaviors of the power system [1–3]. This results in synchronization issues, power-system oscillations, and interactions among various power system equipment [4]. New grid codes specify technical requirements; such as fault ride-through of wind-energy-conversion systems (WECSs) to enrich system security. Low-voltage ride-through (LVRT) refers to the ability of the generator to remain coupled to the system even under low-voltage conditions [5] and to provide reactive power support after the fault clearance. Thus, the transient stability of a grid-connected WECS during severe voltage dip levels on the grid side is a major challenge. It must be verified that wind turbines (WTs) must be reinstated their regular operation properly after the faults.

Given the above, integrating large amounts of WPPs pose new challenges for power systems, which can be overcome by introducing more flexibility when executing the designated functions simultaneously under normal operating conditions. With advanced control designs, the present WT technology is expected to control the power delivered in normal and transient conditions, manage LVRT conditions, and provide additional reactive power for grid support [6]. In contrast, the reactive-power availability is linked to the active power generated. The interactions between turbines and the grid are becoming increasingly important with a large number of variable-speed WTs connected to power networks using wind-power converters (WPCs), which comprise a machine-side converter (MSC), a DC-link, and a grid-side converter (GSC).

B. Literature Review

Permanent-magnet synchronous generators (PMSGs) are promising solutions for WECSs. Owing to the permanent magnets, this configuration does not require an energy supply excitation and provides high power factors and efficiency [7]. The elimination of the gearbox is considered the most significant advantage of PMSG-based WECSs. WTs based on PMSGs have LVRT capabilities and provide a suitable grid connection. This configuration dramatically simplifies the system control structure and reduces the volume and mass of the generator.

During the fault, if the wind-turbine-generator (WTG) does not trip due to protection and continues its grid-connected operation, the WTG terminal voltage will decrease rapidly, and the alternating current of the WPC will rise sharply. In addition, the DC-link voltage will experience a gradual increase [8], and after fault clearance, the WTG terminal voltage rises rapidly to recover its pre-fault level. The WTG's active power gradually recovers, and the DC-link voltage continues to decrease.

The DC-link voltage begins to increase during a high voltage drop at the point-of-common-coupling (PCC), leading to a power imbalance that may destroy the capacitor. Such circumstances enforce the development of improved control designs for WTGs to better contribute to the system stability at drastically reduced voltage levels at the PCC. Conventional WPC controls designed to work reliably under normal conditions are incapable of performing during the worst voltage levels, resulting in a high converter current and its failure. Therefore, it is essential to effectively cater to the effects of the voltage dips at the PCC on the system and treat them economically. The ultimate objective of this study is to propose an efficient control design for WPC-based WTGs aiming to contain the converter (GSC) current

Digital Object Identifier 10.4316/AECE.2022.02008

and DC-link voltage within their designed limits during low-voltage conditions, thus enhancing the LVRT capability of the WTGs.

Several technical solutions addressing these issues are available in the literature. Broadly, these solutions can be classified into two main groups: (1) external hardware-based LVRT methods [9–18] and (2) improved controller-based LVRT methods [19–27]. Hardware-based LVRT methods are further classified into four subgroups [11]: (1) flexible AC transmission system (FACTS) device-based methods, (2) energy storage system (ESS)-based methods, (3) braking chopper (BC)-based methods, and (4) miscellaneous methods. Similarly, improved controller-based LVRT methods can be further categorized into two subgroups: (1) modified converter control-based methods and (2) pitch-angle control (PAC)-based methods.

FACTS devices protect sensitive load from voltage sags, transients, and oscillations [9]. They have the potential in the WT industry to keep the system healthy during disturbances [10-11]. A static synchronous compensator application was suggested in [10] for large-scale integration of wind farms. A dynamic voltage restorer (DVR) can supply and absorb both real and reactive powers and is projected as a potential solution for LVRT enhancement [11]. ESSs are widely used for LVRT improvement of WTGs [12–17]. The authors of [12-13] proposed a superconducting magnetic energy storage (SMES) to mitigate power fluctuations and to enhance the LVRT during grid faults. The application of super-capacitors to improve the transient stability of wind energy systems was proposed in [14-15]. To improve the LVRT capability of a DFIG-based WECS, the authors of [16] combined the properties of DVR and SMES. A BC is an active crowbar method. In [18], the authors suggested a combination of modified converter control and BC control method for a PMSG-based WTG system to handle LVRT operations. Despite the good performance of hardware-based methods in LVRT improvement, higher costs and system complexities are their most significant disadvantages.

Improved converter control-based methods enhance the LVRT capability of WTGs via modified control structures of the WPCs. In [19], the authors proposed a modified converter control structure using a multilevel converter topology. A model predictive control for MSC and GSC to enhance LVRT was presented in [20]. A de-loading droop control approach for a PMSG-based WECS to enhance its LVRT capability was employed in [21]. To improve the LVRT capability of a WT based on PMSG, optimally tuned proportional-integral (PI) regulators and hysteresis current controllers were used in [22] to control the matrix converter. In [23], the MSC was considered to manage the DC-link voltage of a PMSG-based WECS. In [24], a comparison study of various LVRT control techniques was conducted, and some useful directions for their applications were provided. Simple and cost-effective solutions for LVRT operations were achieved using modified converter control methods. However, some of them cannot successfully perform fault ride-through at dramatically reduced voltage levels and require over-sized converters. PAC is widely used in WTs to control the mechanical output power during sudden and excessive wind-speed durations [25]. It was also found to be an effective solution for enhancing the LVRT capability of a PMSG-based WECS [26]. The main disadvantage of this method is its sluggish response during voltage dips at the PCC.

C. Significance of Study

Knowing the limitations of the present LVRT solutions, this study attempted to enrich the existing literature by addressing the drawbacks of the available solutions. To improve the transient stability of a grid-connected WTG and to attain highly reliable system operations at substantially reduced voltage levels, this study presents a revised control design of WPCs, wherein the reference values of the control variables are adjusted according to the voltage level on the grid side and assist the WTG in enhancing its LVRT capability. In the proposed design approach, the excess turbine power during low-voltage conditions is altered into the rotor kinetic energy (*KE*) by regulating the active power of the generator according to the voltage dip level at the PCC. In this situation, the maximum power point tracking (MPPT) operation is interrupted, and the generator's electromagnetic torque and electrical power can be controlled. The proposed control design also contributes to providing the reactive current during LVRT conditions and ensures minimal power loss by utilizing the maximum GSC current-carrying capacity. The overall design supports the GSC containing the fault current within its designed limits.

Compared to existing crowbar methods such as the BC method, etc., the proposed design requires no auxiliary hardware to implement, making it solution cost-effective. In addition, a simplified structure for achieving the enhanced LVRT capability of the WTG under reduced voltage conditions on the grid side validates its feasibility, accuracy, and superior performance. Extensive simulations of a test system with the proposed control design in MATLAB/Simulink are executed to support the above statements. Using the proposed control design, both the transient GSC overcurrent and DC-link overvoltage are successfully restricted in their intended limits. Finally, the control performance of the proposed control design with the other two methods, namely the BC method and PI control method, is compared to demonstrate its effectiveness in achieving highly reliable system operations.

D. Contribution

The contributions of this paper are summarized as follows:

- A simple and cost-effective solution based on an improved control structure of the WPCs for controlling the LVRT operations of PMSG-based WECS wherein the reference values of the control variables are modified according to the voltage conditions at PCC, thus achieving the aims of efficiently controlling the converter current and DC-link voltage within the designed limits;
- Attaining highly reliable system operations at significantly reduced voltage levels on the grid side with trivial oscillations in power generated and power delivered, maintaining system stability, and contributing to system security. Furthermore, the proposed design can provide reactive-current support during LVRT conditions and attempts to minimize

power loss by using the GSC maximum current-carrying capacity.

E. Paper Structure

The remainder of this paper is organized as follows. A brief discussion of the grid-connected direct-drive PMSG-based WECS is presented in Section II. Section III describes the designed procedures for WPCs (i.e., MSC and GSC) to cope with the effects of grid voltage dips and helpful in LVRT enhancement of a PMSG. Afterward, in Section IV, a detailed simulation study for a test system modeled in MATLAB/Simulink is presented and discussed to investigate the feasibility and performance of the proposed control design during voltage dips. Furthermore, the performance of the proposed method is compared to that of two other methods. Finally, conclusions are drawn in Section V.

II. Structure of Grid-Connected PMSG-Based WECS

Figure 1 shows the structure diagram of a grid-connected direct-drive PMSG-based WECS. The WTG with full-rating WPCs can achieve a flexible grid connection. The direct-drive WTG is set up so that the WT directly drives the low-speed synchronous AC machine to generate electrical energy and is directly connected to the grid through the WPCs, thereby improving the system efficiency significantly [23]. Maximum power tracking and pitch angle controls are embedded in the WT control system. A detailed control structure of the PMSG-WTG is omitted here; however, comprehensive mathematical modeling and concepts of a wind-driven PMSG are well explained in [25–27].

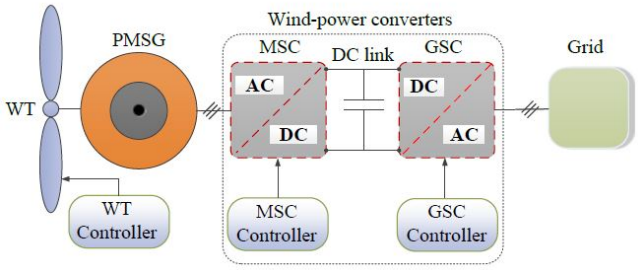

Figure 1. Block diagram of a wind-driven PMSG system

III. Proposed Control Design for LVRT Compliance

This section focuses on the revised WPCs control structure, which is designed to enhance the LVRT capability of a wind-driven PMSG under grid voltage dips. As stated, the prime objectives of this study are to successfully mitigate the GSC overcurrents and DC-link voltage variations during grid disturbances and to ensure the safe and stable operation of the system. These objectives are achieved by establishing revised designs of an MSC and GSC based on modified control variables references according to the voltage dip level at the grid side. Furthermore, the control variables of the revised GSC control structure assist the grid in providing the reactive current. First, the requirements for successful implementation of the LVRT are defined. Following that, the proposed modifications to the MSC and GSC control designs are explained in detail using mathematical concepts, approaches, and analyses.

A. LVRT Requirements

For the successful handling of LVRT, the minimum criteria defined are as follows:

- the stator and grid current limits are restricted to 1.5 times their rated values [2], [28]:

$$|i_s| \le 1.5 I_{s,rated} \quad |i_g| \le 1.5 I_{g,rated} \tag{1}$$

- the possible DC-link voltage variations must be contained in ±15% of its rated value [2], [28]:

$$0.85 V_{dc-ref} \le v_{dc} \le 1.15 V_{dc-ref} \tag{2}$$

The proposed control design, in general, is built on a synchronous reference frame (SRF) with suitable modifications in WPCs, which are explained in the subsequent subsections III-B and III-C.

B. Revised MSC Control Design

The mechanical power (P_m) of the WT is calculated as follows:

$$P_m = P_{gen} + P_{KE} + P_{losses} \tag{3}$$

Under normal operating conditions, the power transferred to the grid (P_{grid}) via GSC and the generator output power (P_{gen}) are equal if losses are not considered, resulting in achieving a stable WT rotor speed and DC-link voltage. However, during a disturbance at the grid side caused by voltage dips, the maximum output of the GSC is reduced to a value depending on the voltage dip level (d) at PCC. This situation results in a power mismatch between P_{grid} and P_{gen}. It is also responsible for increasing the DC-link voltage because the surplus generated power is stored in the DC-link. As a result, the safe and stable operation of WPCs is no longer possible.

To counter this situation and restore the power balance, the power input should also be reduced, which can be carried out by limiting the electromagnetic torque. In this context, the MPPT operation during voltage dips is interrupted, causing the electromagnetic torque to diminish in accordance with the dip level. This eventually reduces the q-axis current immediately. However, it also causes an increase in the rotor speed owing to the torque mismatch in the system. In this regard, (3) becomes

$$P_m = (1-d) P_{gen} + P_{KE} + P_{losses} \tag{4}$$

Instead of converting into generator active power, the turbine input power is stored as the *KE* of the turbine rotor.

$$P_{KE} = J \omega_r \frac{d}{dt} \omega_r \tag{5}$$

In (5), J is the turbine inertia, and ω_r is the rotor speed. Neglecting the friction losses, the increase in the *KE* of the rotor during voltage dips is a function of an increase in rotor speed, and is derived as follows:

$$\Delta KE = \int P_{KE} = J \int_{t_{d,start}}^{t_{d,final}} \omega_r \frac{d}{dt} \omega_r = \\ = \frac{1}{2} J \left[\omega_r^2 \left(t_{d,final} \right) - \omega_r^2 \left(t_{d,start} \right) \right] \tag{6}$$

The stored KE depends on the wind speed, voltage dip level, and dip duration. The worst situation occurs when the system operates at its rated values. In this case, the rotor speed exceeds its maximum limit.

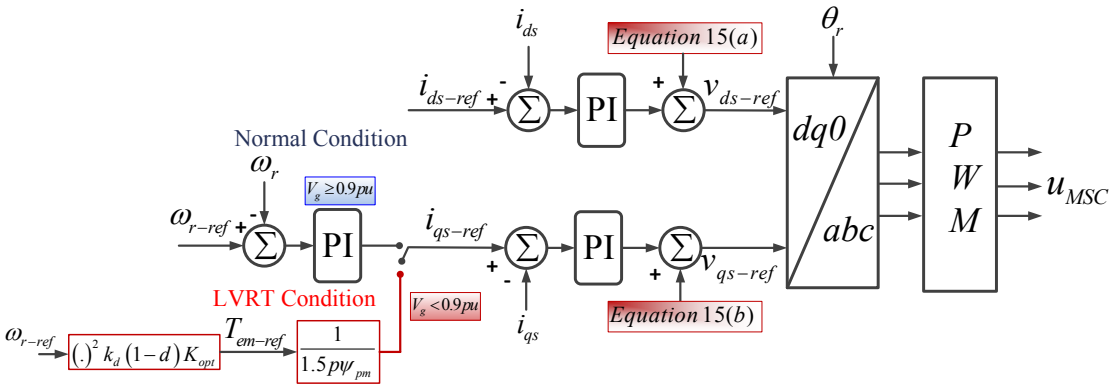

Figure 2. Control scheme of the MSC during grid voltage dips

To tackle this challenging situation, there are two prospective alternatives: 1) de-loading the WT or 2) perturbing the electrical dynamics, which is opted in this study. Efforts are put to establish a relationship between the change in rotor speed ($\Delta\omega_r$) and the voltage dip duration (t_d).

$$\left.\begin{aligned}\omega_{r,final} &= \sqrt{\frac{2\Delta KE}{J}+\omega_{r,start}^2}\\ &= \omega_{r,start}\sqrt{\frac{2\Delta KE}{J\omega_{r,start}^2}+1}\\ &= \omega_{r,start}\sqrt{\frac{t_d}{H}+1}\end{aligned}\right\} H=\frac{J\omega_r^2}{2P_{g,rated}} \quad (7)$$

where, H is the inertia constant of WT. The change in rotor speed is calculated as follows:

$$\omega_{r,final} = \omega_{r,start} + \Delta\omega_{r,td} \quad (8a)$$

$$\left.\begin{aligned}\omega_{r,td} &= \omega_{r,start}\sqrt{\frac{t_d}{H}+1}-1\\ &= \omega_{r,start}\sqrt{\frac{t_d}{H}}\end{aligned}\right. \quad (8b)$$

Under normal operating conditions (d <= 0.1), the rotor speed reference is expressed as follows:

$$\omega_{r-ref} = \frac{V_w}{V_{w,rated}}\omega_{r-rated} \quad (9)$$

In (9), Vw is the wind speed. The reference value of the basic stator-current component (i_{qs-ref}) is directly provided by the speed PI regulator [26].

$$i_{qs-ref} = PI(\omega_{r-ref}-\omega_r), \quad d \leq 0.1 \quad (10)$$

However, during voltage dips (d > 0.1), the rotor speed reference is realized by the following expression:

$$\omega_{r-ref} = \sqrt[2]{\frac{T_{em-ref}}{K_{opt}}} \quad (11)$$

Here, T_{em-ref} is the generator electromagnetic torque reference, and K_{opt} is the design parameters. In this study, the basic stator-current component is controlled to prevent overcurrent in the generator, and the maximum permitted torque inserted into the generator is therefore restricted to a value according to the dip level (d) at the grid side. The analytical expression for the torque injected is given by

$$T_{em-ref} = k_d(1-d)K_{opt}\omega_{r-ref}^2, \quad 0.1 < d < 1 \quad (12)$$

Here, the factor k_d (ϵ [0, 1]), also known as current-suppression factor, is chosen carefully here because it effectively limits transient currents during voltage dips to ensure LVRT control. The reference value of the q-axis stator current (i_{qs-ref}) is expressed as

$$\left.\begin{aligned}i_{qs-ref} &= \frac{1}{1.5p\Psi_{pm}}T_{em-ref}\\ &= \frac{1}{1.5p\Psi_{pm}}k_d(1-d)K_{opt}\omega_{r-def}^2\end{aligned}\right\}, \quad 0.1 < d \leq 1 \quad (13)$$

Analytical expressions for control signals of the MSC are given by

$$v_{ds-ref} = PI(i_{ds-ref}-i_{ds}) + v_{ds-comp.} \quad (14a)$$

$$v_{ds-ref} = PI(i_{qs-ref}-i_{qs}) + v_{qs-comp.} \quad (14b)$$

where, i_{ds-ref} and i_{qs-ref} are the direct (d) and quadrature (q) axes components of stator-current references, respectively; v_{ds-ref} and v_{qs-ref} are the dq-axes stator-voltage references, respectively; $v_{ds-comp.}$ and $v_{qs-comp.}$ are the dq-axes stator-voltage compensation terms, respectively. The d- and q-axis stator voltage compensations terms are expressed by

$$v_{ds-comp} = -\omega_r L_s i_{qs} \quad (15a)$$

$$v_{qs-comp} = \omega_r(L_s i_{ds} + \Psi_{pm}) \quad (15b)$$

In the proposed design, only the voltage at the PCC is involved, and no inertial response is needed during the control procedure. The complete control scheme of the MSC during voltage dips is presented in Fig. 2. Once the voltage recovery stage ends ($V_g \geq 0.9$), the control scheme switches back to its normal operating mode with the aim of MPPT.

C. Revised GSC Control Design

In this subsection, the control designs of the GSC, including the mathematical modeling and detailed analyses under symmetrical and asymmetrical grid voltage dips are presented.

Revised GSC Control – Symmetrical Grid Voltage Dips

As mentioned, the GSC is responsible for the delivery of generated active power to the grid. The unity power-factor operation is achieved under normal grid operations by keeping the reactive-power reference ($Q_{grid-ref}$) of the GSC zero. It is beneficial for reducing converter losses as well. The GSC is controlled using voltage-oriented vector control in which the d-axis direction is the grid-voltage direction and the q-axis rotates 90° along the d shaft.

Accordingly,

$$u_{dg} \cong V_g \quad , \quad u_{qg} = 0 \quad (16)$$

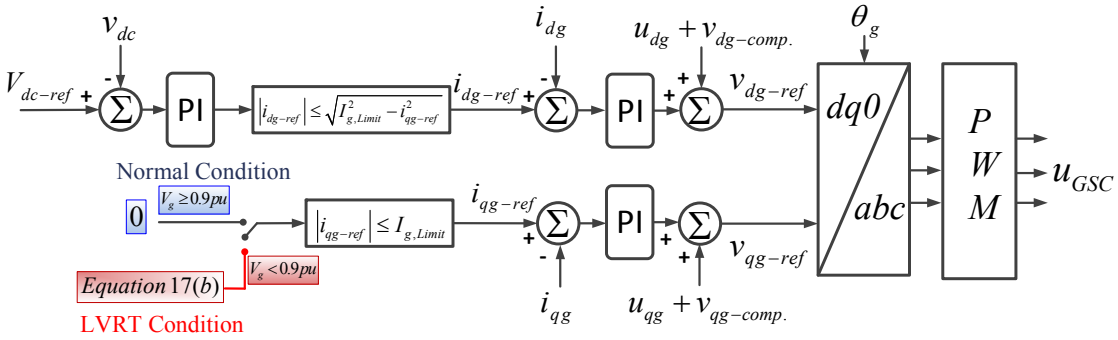

Figure 3. Control scheme of the GSC during symmetrical grid voltage dips

During voltage dips, a reactive current is required in support of the grid voltage. In this context, to comply with the LVRT requirement during voltage dips, the following mathematical expression holds to yield the grid-side reactive-current component (i_{qg-ref}).

$$i_{qg-ref} = 0, \quad d \le 0.1 \tag{17a}$$

$$i_{qg-ref} = dI_{g,rated}, \quad 0.1 < d \le 0 \tag{17b}$$

However, the maximum value of i_{qg-ref} is restricted to rated grid current ($I_{g,rated}$) and is as follows:

$$\left|i_{qg-ref}\right| \le I_{g,rated} \tag{18}$$

The objective of the *d*-axis control of the GSC is to keep a stable DC-link voltage. During voltage dips at the grid side, its function remains unchanged; however, the maximum value of the grid-side current reference (i_{dg-ref}) is restricted to (19) so that the full current-carrying capacity of the GSC can be utilized to minimize the power loss.

$$\begin{aligned} \left|i_{dg-ref}\right| &\le \sqrt{I_{g,Limit}^2 - I_{qg-ref}^2} \\ &\le \sqrt{\left[(1+a)I_{g,rated}\right]^2 - \left[dI_{g,rated}\right]^2} \\ &\le I_{g,rated}\sqrt{(1+a)^2 - d^2} \end{aligned} \tag{19}$$

In (19), *a* is the converter overload capacity factor (in %age). The value of *a* is considered as 10% higher than the maximum grid-side current [25]. The control scheme of the GSC during symmetrical grid voltage dips is presented in Fig. 3. The control signals of the GSC are presented by (20).

$$v_{dg-ref} = PI(i_{dg-ref} - i_{dg}) + v_{dg-comp.} + u_{dg} \tag{20a}$$

$$v_{qg-ref} = PI(i_{qg-ref} - i_{qg}) + v_{qg-comp.} + u_{qg} \tag{20b}$$

$$v_{dg-comp.} = -\omega_g L_g i_{qg} \tag{21a}$$

$$v_{qg-comp.} = \omega_g L_g i_{dg} \tag{21b}$$

where, v_{dg-ref} and v_{gs-ref} are the *dq*-axes grid-side voltage references, respectively; $v_{dg-comp.}$ and $v_{qg-comp.}$ are the *dq*-axes grid-voltage compensation terms, respectively.

Revised GSC Control – Asymmetrical Grid Voltage Dips

Using symmetrical component theory, the unbalanced voltage and current space vectors can be decomposed into their positive- (*p*), negative- (*n*), and zero-sequence components. Because the neutral points of the PMSG are not connected to the grid, the zero-sequence components are nonexistent. Moreover, the PMSG is not directly connected to the grid because the power electronic interface exists between them; therefore, there will be no negative-sequence components in the MSC, and the control design of the MSC is kept similar to that of the asymmetrical grid voltage dips. In this context, pertaining to the asymmetrical grid voltage dips, the control structure of the GSC needs to be modified.

The study of an unbalanced voltage phenomenon is carried out by a positive sequence and a negative sequence. The unbalance problem can be conquered by establishing suitable grid-side *dq* current references to guarantee a well-regulated operation. The control structure (Fig. 4) is replaced by two control loops: the positive-sequence control that works in a positive-sequence SRF, whereas the negative-sequence control performs in a negative-sequence SRF. The control objectives of the positive-sequence and negative-sequence controllers are to regulate the positive sequence and negative sequence grid currents, respectively.

The control function of the positive-sequence loop is similar to that described in the preceding subsection (see subsection III-C). In contrast, the negative sequence grid-side *dq* currents are obtained by filtering off with a notch filter having a frequency of $2f_g$. The filter outputs are controlled to eradicate with the help of negative sequence current controllers having zero current-reference values.

The reference values of the positive-sequence and negative-sequence current components are expressed by

$$i_{dg-ref}^p = PI(V_{dc-link} - v_c) \le \sqrt{\left(I_{g,Limit}\right)^2 - \left(i_{qg-ref}^p\right)^2} \tag{22a}$$

$$i_{qg-ref}^p = dI_{g-rated} \le I_{g,rated}, \quad 0.1 < d \le 1 \tag{22b}$$

$$i_{dg-ref}^n = 0, \quad i_{qg-ref}^n = 0 \tag{22c}$$

where, *p* and *n* are the positive- and negative-sequence components, respectively.

The outputs of the positive-sequence current controllers and the respective compensation terms are expressed as

$$v_{dg-ref}^p = PI(i_{dg-ref}^p - i_{dg}^p) + v_{dg-comp.}^p \tag{23a}$$

$$v_{qg-ref}^p = PI(i_{qg-ref}^p - i_{qg}^p) + v_{qg-comp.}^p \tag{23b}$$

$$v_{dg-ref}^p = -\omega_g L_g i_{qg}^p \tag{24a}$$

$$v_{qg-comp.}^p = \omega_g L_g i_{dg}^p \tag{24b}$$

Similarly, the outputs of the negative-sequence current controllers and the respective compensation terms are

$$v_{dg-ref}^n = PI(i_{dg-ref}^n - i_{dg}^n) + v_{dg-comp.}^n \tag{25a}$$

$$v_{qg-ref}^n = PI(i_{qg-ref}^n - i_{qg}^n) + v_{qg-comp.}^n \tag{25b}$$

$$v_{dg-comp.}^n = \omega_g L_g i_{qg}^n \tag{26a}$$

$$v_{qg-comp.}^n = -\omega_g L_g i_{dg}^n \tag{26b}$$

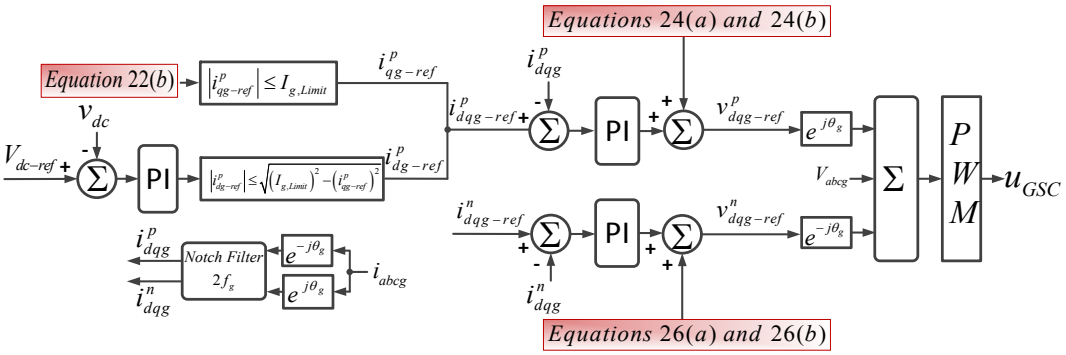

Figure 4. Control scheme of the GSC during asymmetrical grid voltage dips

IV. Simulation Results and Discussions

This section focuses on validating the performance of the proposed control design for LVRT enhancement/improved transient performance of a PMSG-based WECS during severe grid voltage dips. In this context, a simulation model comprised of a 250 kW PMSG-based WT, was built using MATLAB/Simulink, according to Fig. 1.

System parameters are taken from [26] and are listed in Appendix A, including the control parameters. Various types of voltage dips at the grid side, i.e., symmetrical, asymmetrical, and non-instant symmetrical, were applied to the test system.

The results confirm that the system performed adequately in terms of enhancing transient behavior during various voltage dips scenarios. For comparison purposes, the same test system was simulated for two different control methods: the BC and PI control methods, focusing on their LVRT abilities. It is noteworthy to highlight here that the system operated at its rated operating conditions when the various types of grid voltage dips were applied.

A. Control Performance for Symmetrical Grid Voltage Dip

First, a symmetrical voltage dip of 100% in the rated grid voltage for 300 ms at time (t) = 8 s was applied, and the numerical results of the selected transient waveforms are shown in Fig. 5. The control design permits surplus generated power to be stored as the rotor *KE* during-voltage dip. As a result, the rotor accelerates (see Fig. 5) not more than 12% above its rated speed. From this, it can be observed that no active power is delivered to the grid during the dip duration.

The waveform of the generator torque indicates that during the voltage dip, the MPPT operation is interrupted and resumed after the fault clearance when the grid voltage reaches its normal value (V_g >=0.9 pu). During the voltage recovery stage, the rotor speed regains its actual value, and the stored *KE* is delivered to the grid, as illustrated in the waveform of the grid active power (Fig. 5).

During voltage recovery, more power is delivered to the grid since it includes the stored *KE*. In the same graph, the grid reactive power waveform is also presented, which reveals that the reactive power is provided to sustain the grid during the recovery stage. From the graph of the stator current, it can be seen that there are no current spikes after regaining the rated grid voltage, and its magnitude does not violate the criterion defined in (1). The transient outputs of the two most critical quantities, i.e., the DC-link voltage and grid current, are shown in subsection IV.D as these two quantities are selected for comparison purposes.

Given the above analysis, it can be inferred that the proposed control design is proficient in improving the transient performance of the system during a severe symmetrical voltage dip at the PCC. It is noteworthy that there is no possibility of stator overcurrent. As a result, the system remained stable. Thus, it can be included that the proposed design of suitably modifying the reference values of the WPCs control variables during LVRT conditions is a potential solution for LVRT and is promising in wind-power applications.

B. Control Performance for Asymmetrical Grid Voltage Dip

Now, the effects of an asymmetrical grid voltage dip on the simulated test system are discussed. Under the same operating conditions used in the symmetrical voltage dip case, a step single-phase to ground voltage dip of 100% at phase-a was applied. The performance test results of the selected parameters are presented in Fig. 6.

The results are comparable with those obtained during symmetrical voltage dip and ensure that conditions (1) and (2) for the successful implementation of the LVRT are fulfilled.

C. Control Performance for Non-Instant Symmetrical Grid Voltage Dip

In previous cases, it is believed that the voltage drops on the grid side occurred promptly and also the voltage recovery. However, in a real power system, the voltage dip and voltage recovery may be non-instant or multi-staged [29] and are likely to occur. Therefore, this scenario is also studied in order to more firmly claim the suitability of the proposed control design under various voltage dip situations.

Under the same operating conditions as in the two previous cases, a ramp of -5 pu/s (rate of change) with a time duration of 400 ms (beginning at 8 s and finishing at 8.40 s) was applied to the test system to investigate the performance of the proposed design, viewing the dynamics of the selected parameters, as shown in Fig. 7. The results confirm the suitability of the proposed control design in this situation.

From above analyses, it is determined that the transient performance of the PMSG-based WECS is improved with the application of the proposed revised control designs, and the LVRT conditions are effectively handled.

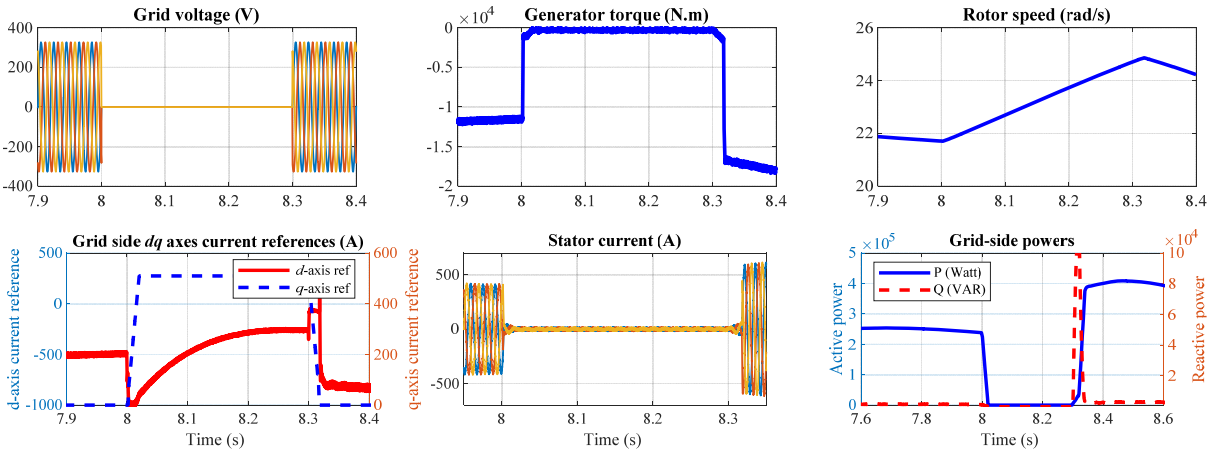

Figure 5. Simulation results under symmetrical grid voltage dip via proposed control design

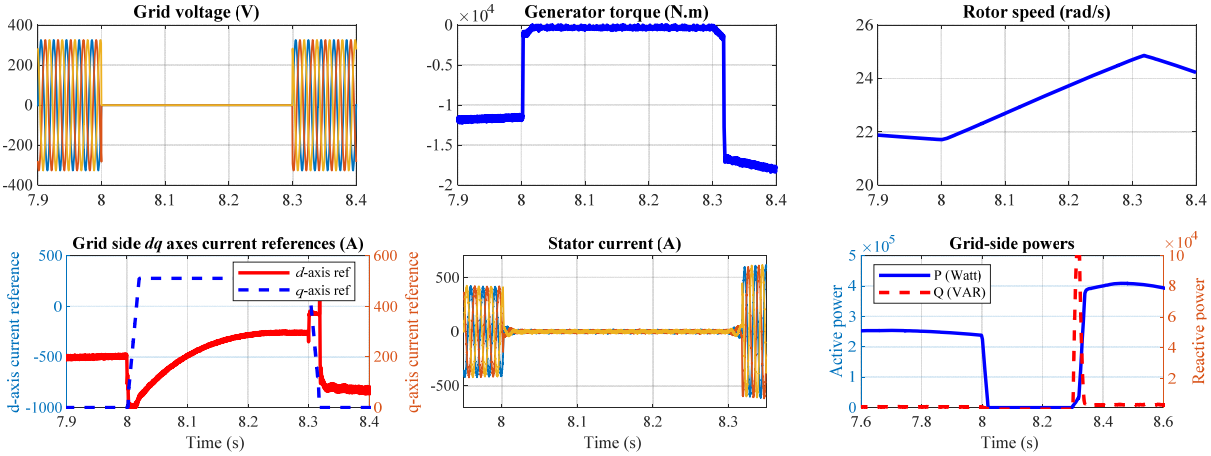

Figure 6. Simulation results under asymmetrical grid voltage dip via proposed control design

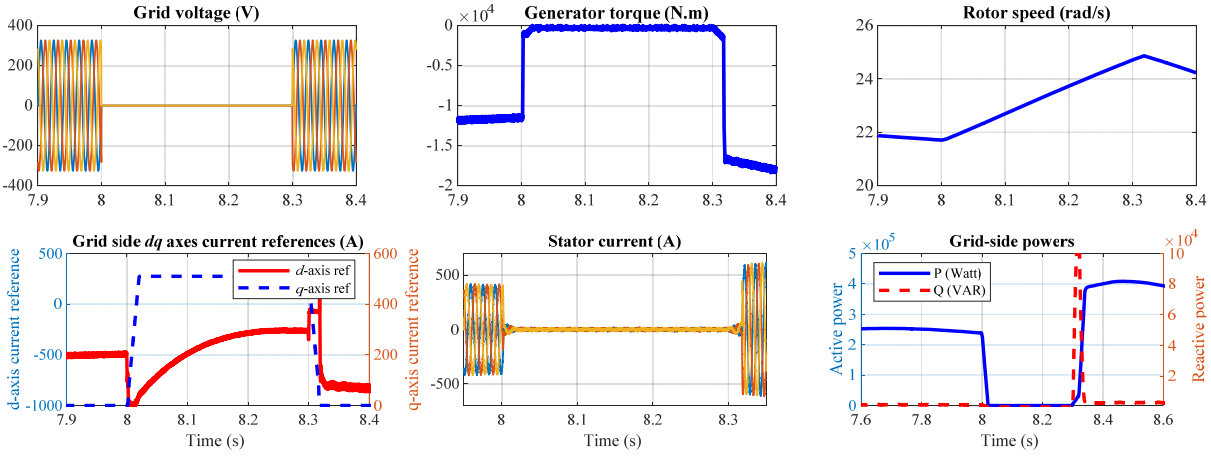

Figure 7. Simulation results under non-instant symmetrical grid voltage dip via proposed control design

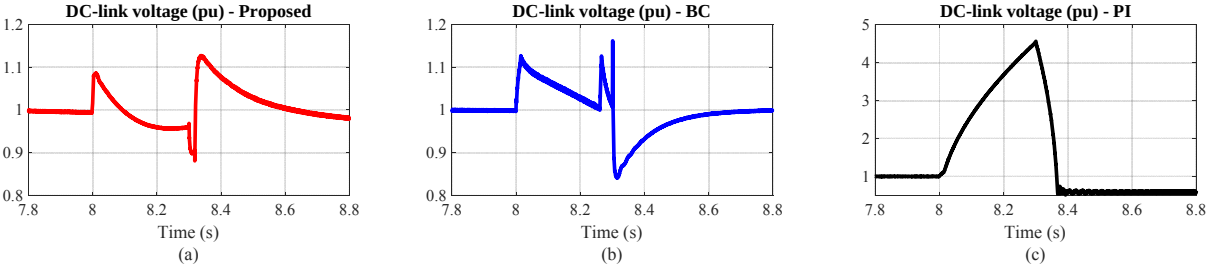

Figure 8. Simulation results of DC-link voltage under symmetrical grid voltage dip: a) proposed method, b) BC method, and c) PI control method

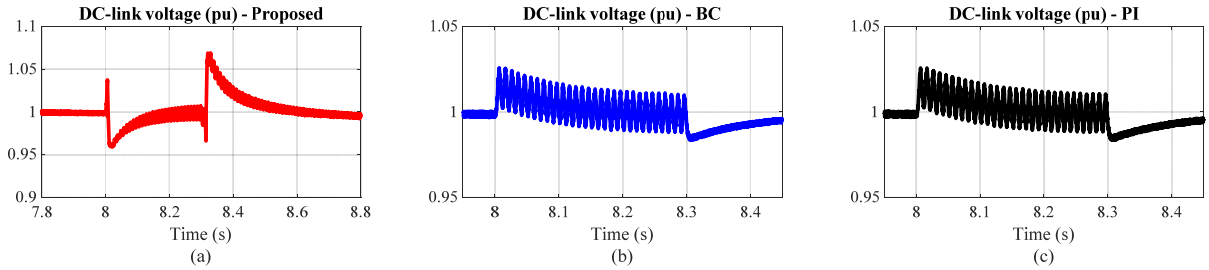

Figure 9. Simulation results of DC-link voltage under asymmetrical grid voltage dip: a) proposed method, b) BC method, and c) PI control method

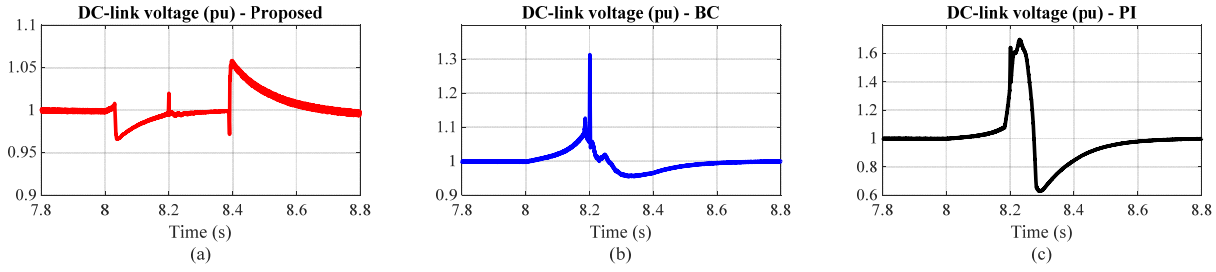

Figure 10. Simulation results of DC-link voltage under non-instant symmetrical voltage dip: a) proposed method, b) BC method, and c) PI control method

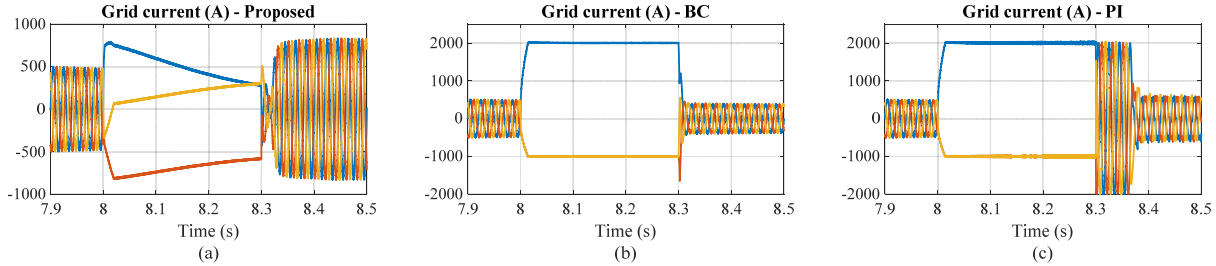

Figure 11. Simulation results of grid current under symmetrical grid voltage dip: a) proposed method, b) BC method, and c) PI control method

D. Control Performance Comparison

A performance comparison of the proposed control design with the BC method and PI control method was performed. Taking the same parameters and conditions, the test system was simulated again using both control methods for earlier cases. For comparison purposes, only two critical parameters, namely DC-link voltage and grid current, were evaluated. Figures 8–10 present the waveforms of the DC-link voltage variations for all three control methods during various voltage dips (symmetrical, asymmetrical, and non-instant symmetrical) at the grid side.

The DC-link voltage waveforms confirm the superior performance of the proposed control design compared to those achieved by the other two methods. Figures 8(c) and 10(c) show that the PI method cannot handle the low-voltage conditions and the DC-link voltage was out of its controllable range. The same happened with the results obtained via the BC control method, as can be observed in Figs. 8(b) and 10(b). However, during the asymmetrical grid voltage dip, the performances of both methods are satisfactory, as can be seen in Figs. 9(b) and 9(c) compared to the proposed control design. Despite having slightly higher variations in the DC-link voltage (see Fig. 9(a)), the result strictly followed the criterion of DC-link voltage limits (2). However, in the case of severe grid voltage dips, the performance of the proposed design is outstanding (see Fig. 8(a) and Fig. 10(a)).

Figures 11–13 present the simulation results of the grid current obtained via three different control methods. During severe dip levels, the amplitude of the grid current is nearly restricted to 1.5 times the rated current when using the proposed control method at the instants of voltage falling and recovery (see Figs. 11(a) and 13(a)), whereas this value exceeds 2 kA in case of other two methods (see Figs. 11 and 13). However, in the case of an asymmetrical voltage dip (see Fig. 12), the other methods also perform better, as the peak value of the current is nearly touched to its limits.

E. Effects of k_d

To highlight the effects of k_d, the test system was simulated again for various values of k_d under a symmetrical grid-voltage dip scenario (see subsection IV.A). However, only the waveforms of the DC-link voltage and grid current are presented here. Figure 14 shows the simulation results of the DC-link voltage, and it can be seen that as voltage falls, the transient DC-link voltage increases with an increase in k_d. During voltage recovery stage, however, the amplitude of the transient DC-link voltage decreases as k_d increases.

The results of the grid current (see Fig. 15) highlight the benefits of using a low value of k_d during voltage falling with respect to the current spike amplitudes. Thus, it is highly recommended to use a low value of k_d during voltage decline and a high value at voltage recovery stage.

V. CONCLUSION

This study addressed the transient problems of a grid-connected wind-driven PMSG under severe voltage dips on the grid side. It proposed an efficient and effective solution based on modified control variables references of the WPCs to enhance the LVRT capacity of the generator. Under the proposed design, the surplus active power was stored in the WT rotor by controlling the active-current component of the generator according to the voltage dip level.

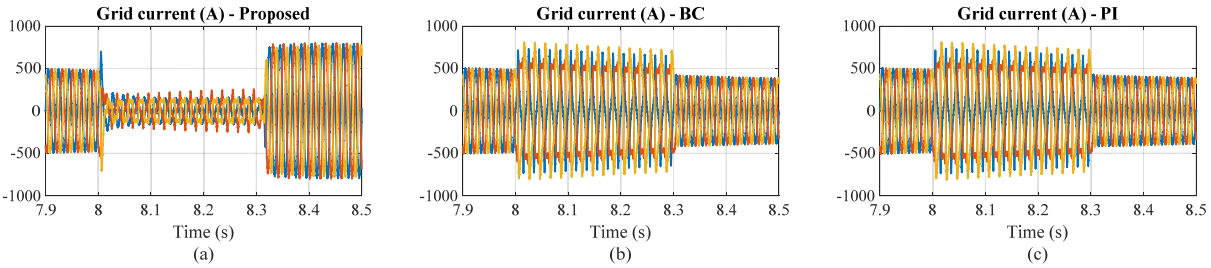

Figure 12. Simulation results of grid current under asymmetrical grid voltage dip: a) proposed method, b) BC method, and c) PI control method

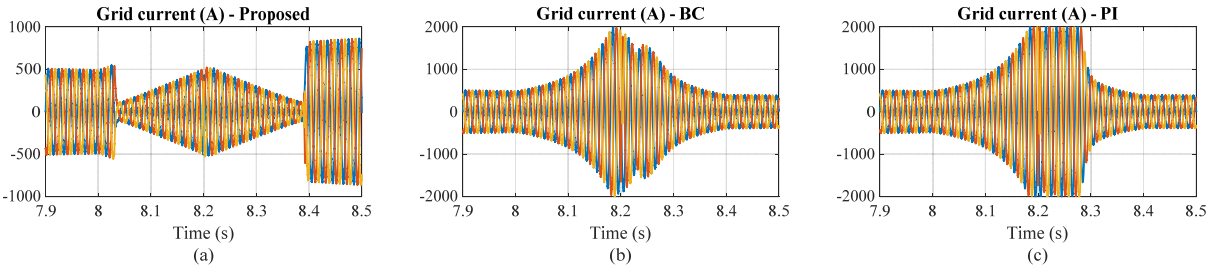

Figure 13. Simulation results of grid current under non-instant symmetrical grid voltage dip: a) proposed method, b) BC method, and c) PI control method

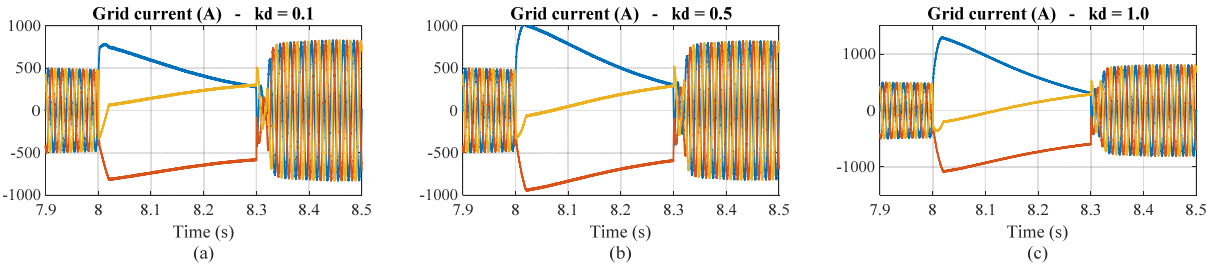

Figure 14. Simulation results of DC-link voltage under symmetrical voltage dip for different values of k_d: (a) $k_d = 0.1$, (b) $k_d = 0.5$, and (c) $k_d = 1.0$

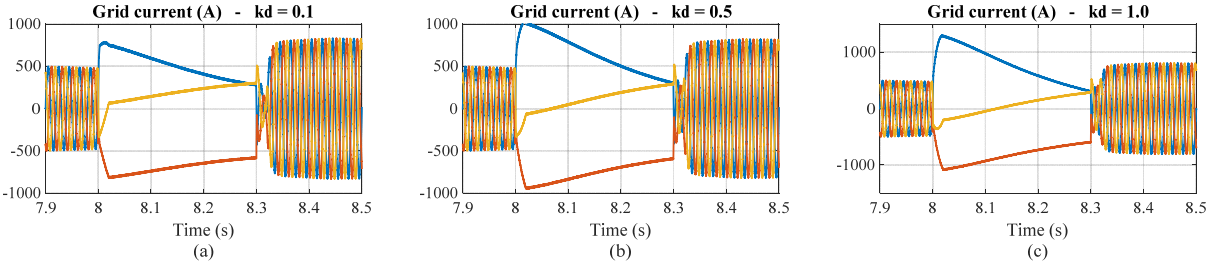

Figure 15. Simulation results of grid current under symmetrical voltage dip for different values of k_d: (a) $k_d = 0.1$, (b) $k_d = 0.5$, and (c) $k_d = 1.0$

The GSC control managed the DC-link voltage and grid current within their safe operating limits (1) and (2). The revised control design of the WPCs also contributed to providing reactive-power support during voltage recovery and attempted to minimize the power loss by utilizing the maximum GSC current-carrying capacity. Following conclusions are drawn:

1. The WECS remained firmly connected to the grid during severe voltage dips with trivial oscillations in power generated and power delivered; therefore, making this control design acceptable for wind-power applications;
2. With the help of the proposed design, not only the DC-link voltage but also the grid current persisted within their defined boundaries, confirming its suitability in attaining the system reliability and stability;
3. The proposed design provided reactive power support during voltage recovery;
4. The control performance comparison revealed the enhanced system's transient performance using the proposed control design under different dip levels, showing that the system's dynamic performance improved substantially.
5. Having a simplified control structure requiring no additional hardware made this solution feasible, cost-effective, and promising in the WT industry.

APPENDIX A

TABLE I. PARAMETERS OF 250KW WT SYSTEM

Parameters	Value	Unit
Rated turbine power	250	kW
Air density	1.225	kg/m^3
Turbine radius	14.26	m
Rated wind speed	11	m/s
Optimal TSR for MPPT	8.1	-
Maximum power coefficient	0.48	-

TABLE II. PARAMETERS OF 280KW PMSG SYSTEM

Parameters	Value	Unit
Rated generator power	280	kW
Pole pair number	18	Nos.
Stator winding resistance	0.04	Ω
Stator winding inductance	0.835	mH
Rated toque	12.818	kN.m
Rotational inertia	1000	kg.m^2
Permanent magnetic flux	1.052	V.s
Viscous damping	2.5	N.m.s
Rated stator current	448	A
Maximum stator current	672.12	A

TABLE III. GRID DATA

Parameters	Value	Unit
Rated grid voltage (phase-phase)	400	V (rms)
Rated current	571.55	A
Maximum grid-side current	857.32	A
Rated frequency	50	Hz
DC-link voltage reference	1200	V
DC-link capacitance	3.75	mF
Grid-side filter resistance	12.6	mΩ
Grid-side filter inductance	0.8	mH

TABLE IV. CONTROLLER DATA

Controllers	K_P	K_i
Current controllers	0.4	12
Speed controller	30	300
DC-link voltage controller	10	100

REFERENCES

[1] M. A S. Ali, "Utilizing active rotor-current references for smooth grid connection of a DFIG-based wind-power system," Advances in Electrical and Computer Engineering, vol. 20, no. 4, pp. 91-98, 2020. doi:10.4316/AECE.2020.04011

[2] M. A. S. Ali, K. K. Mehmood, S. Baloch, C. H. Kim, "Modified rotor-side converter control design for improving the LVRT capability of a DFIG-based WECS," Electric Power Systems Research, vol. 186, p. 106403, 2020. doi:10.1016/j.epsr.2020.106403

[3] M. A S. Ali, "Step towards enriching frequency support from wind-driven permanent-magnet synchronous generator for power system stability," Advances in Electrical and Computer Engineering, vol. 22, no. 1, pp. 77-86, 2022. doi:10.4316/AECE.2022.01009

[4] M. A. S. Ali, "LMI-based state feedback control structure for resolving grid connectivity issues in DFIG-based WT systems," Eng, vol. 2, no. 4, pp. 562-591, 2021. doi:10.3390/eng2040036

[5] M. A S. Ali, K. K. Mehmood, J. S. Kim, C. H. Kim, "ESD-based Crowbar for Mitigating DC-link Variations in a DFIG-based WECS," In: International Conference on Power System Transients, Perpignan, France, pp. 1-6, 2019

[6] M. Firouzi, G. B. Gharehpetian, "LVRT performance enhancement of DFIG-based wind farms by capacitive bridge-type fault current limiter," IEEE Transactions on Sustainable Energy, vol. 9, no. 3, pp. 1118-1125, 2018. doi:10.1109/TSTE.2017.2771321

[7] M. J. Dehkordi, S. V. Zadeh, J. Mohammadi, "Development of a combined control system to improve the performance of a PMSG-based wind energy conversion system under normal and grid fault conditions," IEEE Transactions on Energy Conversion, vol. 34, no. 3, pp. 1287-1295, 2019. doi:10.1109/TEC.2019.2912080

[8] O. P. Mahela, N. Gupta, M. Khosravy, N. Patel, "Comprehensive overview of low voltage ride through methods of grid integrated wing generator," IEEE Access, vol. 7, pp. 99299-99326, 2019. doi:10.1109/ACCESS.2019.2930413

[9] M. A. S. Ali, K. K. Mehmood, C. H. Kim, "Power system stability improvement through the coordination of TCPS-based damping controller and power system stabilizer," Advances in Electrical and Computer Engineering, vol. 17, no. 4, pp. 27-36, 2017. doi:10.4316/AECE.2017.04004

[10] H. Geng, L. Liu, R. Li, "Synchronization and reactive current support of PMSG-Based wind farm during severe grid fault," IEEE Transactions on Sustainable Energy, vol. 9, no. 4, pp. 1596-1604, 2018. doi:10.1109/TSTE.2018.2799197

[11] M. F. Kangarlu, E. Babei, F. Blaabjerg, "A comprehensive review of dynamic voltage restorer," International Journal of Electrical Power and Energy System, vol. 92, pp. 135-155, 2019. doi:10.1016/j.ijepes.2017.04.013

[12] Z. Salama, H. S. Aly, M. M. Abdel-Akher, M. et al., "Frequency and voltage control of microgrid with high WECS penetration during wind gusts using superconducting magnetic energy storage," Electrical Engineering, vol. 101, pp. 771-786, 2019. doi:10.1007/s00202-019-00821-w

[13] C. Huang, X. Y. Xiao, Z. Zheng, Y. Wang, "Cooperative control of SFCL and SMES for protecting PMSG-Based WTGs under grid faults," IEEE Transactions on Applied Superconductivity, vol. 29, no. 2, p. 5601106, 2019. doi:10.1109/TASC.2019.2891908

[14] M. N. Musarrat, A. Fekih, "A fractional order sliding mode control-based topology to improve the transient stability of wind energy systems," International Journal of Electrical Power and Energy System, vol. 133, p. 107306, 2021. doi:10.1016/j.ijepes.2021.107306

[15] M. K. Döşoğlu, O. Özkaraca, U. Güvenç, "Novel active–passive compensator–supercapacitor modeling for low-voltage ride-through capability in DFIG-based wind turbines," Electrical Engineering, vol. 101, pp. 1119-1132, 2019. doi:10.1007/s00202-019-00857-y

[16] M. N. Musarrat, A. Fekih, M. R. Islam, "An improved fault ride through scheme and control strategy for DFIG-based wind energy systems," IEEE Transactions on Applied Superconductivity, vol. 31, no. 8, p. 5401906, 2021. doi:10.1109/TASC.2021.3096181

[17] M. A. S. Ali, K. K. Mehmood, J. K. Park, C. H. Kim, "Battery energy storage system-based stabilizers for power system oscillations damping," Journal of the Korean Institute of Illuminating and Electrical Installation Engineers, vol. 10, pp. 75-84, 2016. doi:10.5207/JIEIE.2016.30.10.075

[18] P. Xing, L. Fu, G. Wang, Y. Zhang, "A composite control method of low-voltage ride through for PMSG-based wind turbine generation system," IET Generation, Transmission and Distribution, vol. 12, no. 1, pp. 117-125, 2018. doi:10.1049/iet-gtd.2017.0270

[19] M. Wang, Y. Hu, W. Zhao, Y. Wang, G. Chen, "Application of modular multilevel converter in medium voltage high power permanent magnet synchronous generator wind energy conversion systems," IET Renewable Power Generation, vol. 10, no. 16, pp. 824-833, 2016. doi:10.1049/iet-rpg.2015.0444

[20] L. S. Barros, C. M. V. Barros, "An internal model control for enhanced grid-connection of direct-driven PMSG-based wind generators," Electric Power Systems Research, vol. 51, pp. 440-450, 2017. doi:10.1016/j.epsr.2017.06.014

[21] O. A. Lara, N. Jenkins, J. Ekanayake, P. Cartwright, F. Hughes, Wind energy generation: Modeling and Control, Wiley, 2009

[22] N. H. Saad, A. A. El-Sattar, M. E. Marei, "Improved bacterial foraging optimization for grid connected wind energy conversion system based PMSG with matrix converter," Ain Shams Engineering Journal, vol. 9, no. 4, pp. 2183-2193, 2018. doi:10.1016/j.asej.2017.03.010

[23] Z. M. Hailemariam, R. Leidhold, G. T. Tesfamariam, Real-time dc-link voltage control of 5-kW PMSG-based wind turbine generator through a test-rig," Electrical Engineering, vol. 103, pp. 1869-1880, 2021. doi:10.1007/s00202-020-01176-3

[24] R. Basak, G. Bhuvaneswari, R. Pillai, "Low-voltage ride-through of a synchronous generator-based variable speed grid-interfaced wind energy conversion system," IEEE Transactions on Industry Applications, vol. 56, no. 1, pp. 752-762, 2020. doi:10.1109/TIA.2019.2946125

[25] M. A. S. Ali, K. K. Mehmood, C. H. Kim, "Full operational regimes for SPMSG-based WECS using generation of active current references," International Journal of Electrical Power and Energy System, vol. 112, pp. 428–441, 2019. doi:10.1016/j.ijepes.2019.05.028

[26] M. A. S. Ali, K. K. Mehmood, S. Baloch, C. H. Kim, "Wind-speed estimation and sensorless control for SPMSG-based WECS using LMI-based SMC," IEEE Access, vol. 8, pp. 26524-26535, 2020. doi:10.1109/ACCESS.2020.2971721

[27] X. Q. Zhang, J. He, Y. Xu, Z. Hong, Y. Chen, K. Strunz, "Average-value modeling of direct-driven PMSG-based wind energy conversion systems," IEEE Transactions on Energy Conversion, pp. 1-1, 2021. doi:10.1109/TEC.2021.3095486

[28] Y. Shen, D. Ke, Y. Sun, D. S. Kirschen, W. Qiao, X. Deng, "Advanced auxiliary control of an energy storage device for transient voltage support of a doubly fed induction generator," IEEE Transactions on Sustainable Energy, vol. 7, no. 1, pp. 63-76, 2016. doi:10.1109/TSTE.2015.2472299

[29] F. Blaabjerg, D. Xu, W. Chen, N. Zhu, Advanced control of doubly fed induction generator for wind power systems, Wiley-IEEE, 2018